

## DEEP $u^*$ - AND $g$ -BAND IMAGING OF THE *SPITZER SPACE TELESCOPE* FIRST LOOK SURVEY FIELD: OBSERVATIONS AND SOURCE CATALOGS

HYUNJIN SHIM,<sup>1</sup> MYUNGSHIN IM,<sup>1</sup> SOOJONG PAK,<sup>2,3</sup> PHILIP CHOI,<sup>4</sup> DARIO FADDA,<sup>4</sup>  
GEORGE HELOU,<sup>4</sup> AND LISA STORRIE-LOMBARDI<sup>4</sup>  
*Received 2006 January 31; accepted 2006 February 24*

### ABSTRACT

We present deep  $u^*$ - and  $g$ -band images taken with the MegaCam on the 3.6 m Canada-France-Hawai'i Telescope to support the extragalactic component of the *Spitzer* First Look Survey (FLS). In this paper we outline the observations, present source catalogs, and characterize the completeness, reliability, astrometric accuracy, and number counts of this data set. In the central 1 deg<sup>2</sup> region of the FLS, we reach depths of  $g \sim 26.5$  mag and  $u^* \sim 26.2$  mag (AB magnitude,  $5\sigma$  detection over a  $3''$  aperture) with  $\sim 4$  hr of exposure time for each filter. For the entire FLS region ( $\sim 5$  deg<sup>2</sup> coverage), we obtained  $u^*$ -band images to the shallower depth of  $u^* = 25.0$ – $25.4$  mag ( $5\sigma$ ,  $3''$  aperture). The average seeing of the observations is  $0''.85$  for the central field and  $\sim 1''.00$  for the other fields. Astrometric calibration of the fields yields an absolute astrometric accuracy of  $0''.15$  when matched with the SDSS point sources between  $18 < g < 22$ . Source catalogs have been created using SExtractor. The catalogs are 50% complete and  $>99.3\%$  reliable down to  $g \simeq 26.5$  mag and  $u^* \simeq 26.2$  mag for the central 1 deg<sup>2</sup> field. In the shallower  $u^*$ -band images, the catalogs are 50% complete and 98.2% reliable down to 24.8–25.4 mag. These images and source catalogs will serve as a useful resource for studying the galaxy evolution using the FLS data.

*Subject headings:* catalogs — galaxies: photometry — surveys

### 1. INTRODUCTION

Since its launch in 2003 August, the *Spitzer Space Telescope* has opened new IR observing windows to the universe and probed to unprecedented depths. The first scientific observation undertaken with *Spitzer* after its in-orbit-checkout period was the *Spitzer* First Look Survey (FLS). The survey provided the first look of the mid-infrared (MIR) sky with deeper sensitivities than previous systematic large surveys,<sup>5</sup> allowing future users to gauge *Spitzer* sensitivities. For the extragalactic component of the FLS, the  $\sim 4.3$  deg<sup>2</sup> field centered at R.A.(J2000.0) =  $17^{\text{h}}18^{\text{m}}00^{\text{s}}$ , decl.(J2000.0) =  $+59^{\circ}30'00''$  was observed with the Infrared Array Camera (IRAC; 3.6, 4.5, 5.8, 8.0  $\mu\text{m}$ ; Fazio et al. 2004) and the Multiband Imaging Photometer for *Spitzer* (MIPS; 24, 70, 160  $\mu\text{m}$ ; Rieke et al. 2004). The main survey field has flux limits of 20, 25, 100, and 100  $\mu\text{Jy}$  at wavelengths of IRAC 3.6, 4.5, 5.8, and 8.0  $\mu\text{m}$ , respectively. The deeper verification field, covering the central 900 arcmin<sup>2</sup> field, has sensitivities of 10, 10, 30, and 30  $\mu\text{Jy}$  at IRAC wavelengths (Lacy et al. 2005). Also, the FLS verification strip field has  $3\sigma$  flux limits of 90  $\mu\text{Jy}$  at MIPS 24  $\mu\text{m}$  (Yan et al. 2004a) and 9 and 60 mJy at 70 and 160  $\mu\text{m}$  (Frayer et al. 2006). The reduced images and source catalogs have been released (Lacy et al. 2005; Frayer et al. 2006).

In order to support the FLS, various ground-based ancillary data sets have also been obtained. A deep  $R$ -band survey to  $R_{\text{AB}}(5\sigma) = 25.5$  mag (KPNO 4 m; Fadda et al. 2004) and a radio survey at 1.4 GHz to 90  $\mu\text{Jy}$  (VLA; Condon et al. 2003) have been performed to identify sources at different wavelengths. Im-

aging surveys with the Palomar Large Format Camera (LFC),  $g'$ -,  $r'$ -,  $i'$ -, and  $z'$ -band data covering 1–4 deg<sup>2</sup> have also been taken since 2001. The Sloan Digital Sky Survey (SDSS) also covers the FLS field. Moreover, spectroscopic redshifts have been obtained for many sources using the Deep Imaging Multi-Object Spectrograph (DEIMOS) at the Keck observatory, as well as the Hydra instrument on the Wisconsin Indiana Yale NOAO (WIYN) observatory. Utilizing all the *Spitzer* and the ground-based ancillary data sets, many science results have come out already from the FLS. The FLS studies range from the infrared source counts to the properties of obscured galaxies such as submillimeter galaxies, red active galactic nuclei (AGNs), and extremely red objects (e.g., Yan et al. 2004b; Fang et al. 2004; Marleau et al. 2004; Frayer et al. 2004; Appleton et al. 2004; Lacy et al. 2004; Choi et al. 2006).

In order to broaden the scientific scope of the FLS, we have obtained new ground-based ancillary data sets, deep  $u^*$ -band and  $g$ -band imaging data that will be presented in this paper. The exploration of the cosmic star formation history at  $z \lesssim 3$  is one of the key scientific issues that the FLS is designed to address. While studying the infrared emission is an extremely valuable way to understand the obscured star formation history of the universe, a complete census of the cosmic star formation history requires the measurement of unobscured star formation as well. Such a measurement can be done effectively using the rest-frame ultraviolet (UV) continuum, which represents either instantaneous star formation activity of massive stars (far-UV [FUV]), or traces the star formation from intermediate-age stars (near-UV [NUV]; Kennicutt 1998). The FUV and NUV emission of galaxies at  $z \lesssim 1$  redshifts to the  $u$  band; therefore, the addition of the  $u$  band enables us to describe the star formation history at  $z \lesssim 1$  to the full extent. Also, using the deep  $u$ - and  $g$ -band data, it is possible to select  $u$ -band dropout galaxies—star-forming galaxies at  $z \sim 3$ . Especially of interest are bright, massive Lyman break galaxies (LBGs), which are rare but are important to constrain galaxy evolution models since they can tell us how massive galaxies are assembled in the early universe. The wide area coverage of the FLS allows us to

<sup>1</sup> Department of Physics and Astronomy, Seoul National University, Seoul, South Korea; hjshim@astro.snu.ac.kr, mim@astro.snu.ac.kr.

<sup>2</sup> Korea Astronomy and Space Science Institute, Daejeon, South Korea.

<sup>3</sup> Department of Astronomy and Space Science, Kyung Hee University, Gyeonggi-do 446-701, South Korea.

<sup>4</sup> *Spitzer* Science Center, California Institute of Technology, Pasadena, CA 91125.

<sup>5</sup> See the First Look Survey Web site, <http://ssc.spitzer.caltech.edu/fls>.

TABLE 1

CHARACTERISTICS OF THE FILTERS USED IN megacam OBSERVATIONS

Characteristic	$u^*$ Filter	$g$ Filter
Central wavelength (Å) .....	3740	4870
Wavelength range (Å).....	3370–4110	4140–5590
Mean transmission .....	69.7%	84.6%

select such rare, bright LBGs. However, for the selection of LBGs, it is necessary to obtain  $u$ - and  $g$ -band data that matches the depth of the *Spitzer* data. In addition, the  $u$ - and  $g$ -band data sets can be used to test extinction correction methods, such as the estimation of dust extinction based on the measurement of UV slope (Calzetti et al. 1994; Meurer et al. 1999; Adelberger & Steidel 2000). When used together with other ground-based ancillary data, our  $u$ - and  $g$ -band data will be very helpful for improving the accuracy of photometric redshifts.

With these scientific applications in mind, we present the  $u^*$ - and  $g$ -band optical observations made with the MegaCam at the Canada France Hawaii Telescope (CFHT). The data set is composed of (1) deep  $u^*$ - and  $g$ -band data for the central  $1 \text{ deg}^2$  of the FLS and (2)  $u^*$ -band data for the whole FLS. In § 2, we describe how our observations were made. The reduction and calibration procedures are in § 3. Production of source catalogs is described in § 4. Finally, in § 5, we show the properties of the final images and the extracted catalogs. Throughout this paper, we use AB magnitudes (Oke 1974).

## 2. OBSERVATIONS

The observations were made using the MegaCam on the 3.6 m Canada France Hawaii Telescope (CFHT). MegaCam consists of 36  $2048 \times 4612$  pixel CCDs, covering  $0.96 \times 0.94$  field of view with a resolution of  $0''.187 \text{ pixel}^{-1}$  (see the detailed description in Boulade et al. 2003). The available broadband filters are similar to SDSS *ugriz* filters, but not exactly the same, especially in the case of the  $u^*$  band. We used  $u^*$  and  $g$  filters for our observations. The filter characteristics are summarized in Table 1, and their response curves are compared with the SDSS  $u$ - and  $g$ -band filters in Figure 1. Note that these response curves include the quantum efficiency of the CCDs. The response curves of the two  $g$  bands are nearly identical in their shapes, but the  $u^*$ -band response curve shows a different overall shape compared with the SDSS  $u$  band, in such a sense that the  $u^*$  filter is redder than SDSS  $u$ . The difference leads to as much as a 0.6 mag difference between the CFHT and SDSS  $u$  magnitudes. This will be investigated further in the photometry section (§ 5.2).

Our images on the FLS field were taken with the queued observation mode in two separate runs (03B and 04A semesters). The first observing run occurred in 2003 August 23–29 ( $u^*$  band) and 2003 September 19–22 ( $g$  band). During this 03B run, we observed the central  $1 \text{ deg}^2$  of the FLS field, which covers the entire FLS verification strip. Images are taken with medium dither steps of about  $30''$ , at 12 ( $u^*$ ) or 20 ( $g$ ) different dither positions. The exposure time at each position was 1160 s for the  $u^*$  band and 680 s for the  $g$  band. Therefore, the total integration time per pixel amounts to  $\sim 3.8$  hr for both bands. The yellow box in Figure 2 shows the location of this deep  $u^*$ - and  $g$ -band data superimposed on the  $R$ -band images (Fadda et al. 2004).

In the second observing run during 04A period, we obtained  $u^*$ -band images covering the whole FLS field ( $\sim 5 \text{ deg}^2$ ) at a shallower depth. Note that we did not take  $g$ -band data because the entire FLS is covered to a shallower depth by the existing  $g$ -band data taken with the Palomar 5 m telescope. The CFHT observa-

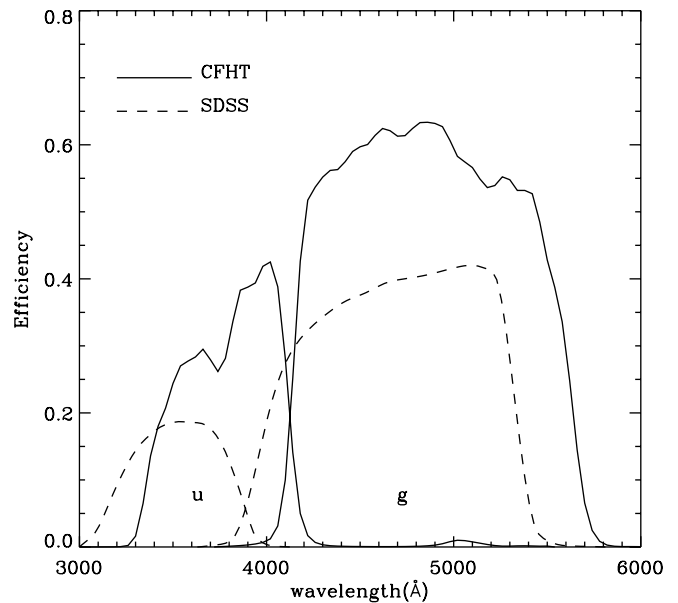


FIG. 1.—Response curves of CFHT  $u^*$  and  $g$  filters multiplied by the telescope (mirror, optics) and CCD efficiency (solid lines). The CFHT data points are taken from a CFHT-related Web site (<http://astrowww.phys.uvic.ca/grads/gwyn/cfhtls>). The SDSS  $u$ - and  $g$ -band transmission curves are given as dashed lines (<http://www.sdss.org>). The CFHT filters are slightly redder than their SDSS counterparts.

tion was at first designed to take 10 dithered images at 7 different locations of the FLS area, which are named FLS11–FLS32 (Table 2). The cyan boxes marked with the dashed line in Figure 2 indicate FLS11–FLS32 fields. The dates of the observations span quite a wide range from 2004 April to July. Some of the fields have all dithered images observed on a photometric condition (FLS21, FLS22, and FLS31), but other fields contain the images that are nonphotometric. Due to the bad weather, we lost some of the queued observing time and several observed images were not validated. Each dithered image was taken with the exposure time of 680 s. Although the original plan was to achieve 1.9 hr of total integration at each location, there is a field-to-field variation on the image depth between  $\sim 1$  and  $\sim 2$  hr. Table 2 gives the summary of the 03B and 04A observations. The seeing condition of the whole observation sessions ranged from  $0''.85$  to  $1''.08$ .

Between 2003 August and September, one of the 36 MegaCam CCDs was malfunctioning. As a result,  $g$ -band images lack [CCD03] part of the observed field. Hence, the effective survey area in co-added mosaic images is  $\sim 0.94 \text{ deg}^2$  for the central field.

## 3. DATA REDUCTION

### 3.1. Preprocessing with Elixir

All MegaCam data obtained at CFHT are preprocessed through the Elixir pipeline,<sup>6</sup> the standard pipeline for the basic reduction of the MegaCam data, provided by the CFHT. Through the Elixir pipeline, the raw object frames are bias-subtracted, flat-fielded, and photometrically calibrated. In the Elixir photometric calibration, the nightly photometric zero point is estimated using the standard star data on that night. Basic astrometric calibrations are done using  $\sim 50$ – $60$  USNO (United States Naval Observatory catalog; Zacharias et al. 2000) and *HST* GSC (*Hubble Space Telescope* Guide Star Catalog; Morrison et al. 2001) reference stars per chip. In this calibration, the average pixel scale and the

<sup>6</sup> See the Elixir Web site, <http://www.cfht.hawaii.edu/Instruments/Elixir>.

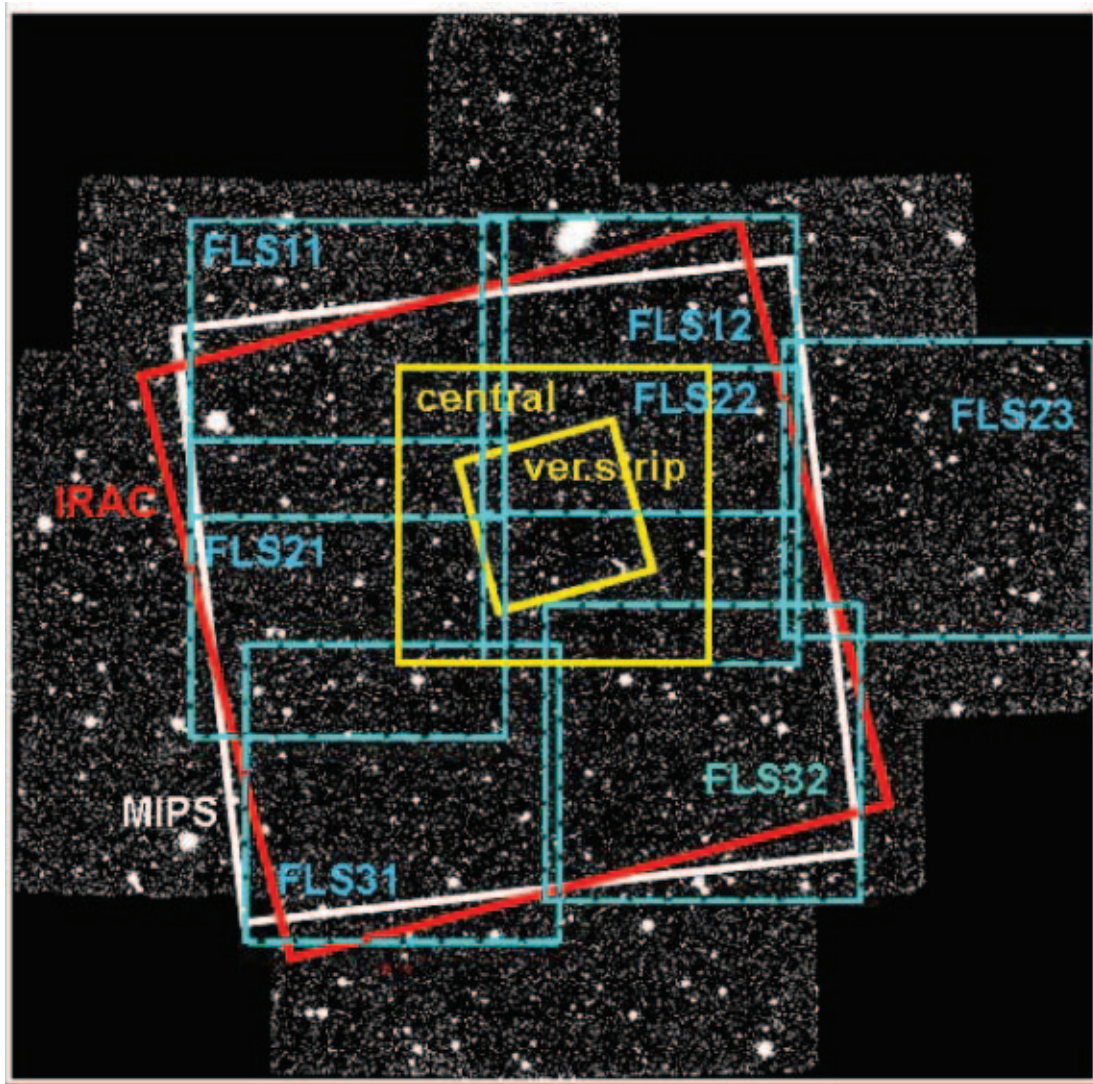


FIG. 2.—Area coverages of various data sets over the FLS. The small yellow square in the center represents the *Spitzer* FLS verification strip, and the big yellow square shows our CFHT observations in the central 1 deg<sup>2</sup>. The red and white squares correspond to the whole FLS area (IRAC and MIPS, respectively), which covers  $\sim 4.3$  deg<sup>2</sup>. The cyan squares indicate the area covered by our CFHT  $u^*$ -band observations in 2004. All these marks are overlaid on the KPNO  $R$ -band images.

TABLE 2  
OBSERVATION SUMMARY

Field ID	R. A. (J2000.0)	Decl. (J2000.0)	Observation Dates	Filter	Total Exposure Time (s)	Depth (AB mag) <sup>a</sup>	Seeing (arcsec) <sup>b</sup>	Zero Point <sup>c</sup>
Central.....	17 17 01	+59 45 08	2003 Aug 25, 2003 Aug 29	$u^*$	1160 × 12	26.41	0.85	32.904
Central.....	17 17 01	+59 45 08	2003 Sep 19, 2003 Sep 21, 2003 Sep 22	$g$	680 × 20	26.72	0.85	33.430
FLS11.....	17 22 09	+60 14 47	2004 Apr 29, 2004 Jul 12	$u^*$	680 × 10	25.83	0.98	32.226
FLS12.....	17 14 44	+60 14 50	2004 Jun 18, 2004 Jul 17	$u^*$	680 × 9	25.85	1.06	32.186
FLS21.....	17 22 14	+59 30 00	2004 Jul 10, 2004 Jul 21	$u^*$	680 × 9	25.91	0.98	32.236
FLS22.....	17 14 47	+59 44 45	2004 Jul 10	$u^*$	680 × 5	25.57	1.08	32.213
FLS23.....	17 07 09	+59 48 26	2004 Jul 11	$u^*$	680 × 5	25.43	0.89	32.221
FLS31.....	17 20 46	+58 49 09	2004 Jul 11, 2004 Jul 22	$u^*$	680 × 8	25.68	0.90	32.188
FLS32.....	17 13 32	+58 57 46	2004 Jul 12	$u^*$	680 × 7	25.67	0.95	32.139

NOTE.—Units of right ascension are hours, minutes, and seconds, and units of declination are degrees, arcminutes, and arcseconds.

<sup>a</sup> The depth of a field is calculated as  $5\sigma$  flux over a  $3''$  aperture.

<sup>b</sup> The seeing of the image was determined through a visual inspection of individual stars.

<sup>c</sup> The zero points are calibrated from original Elixir photometric solution (see § 3.5). The values are given as zero points according to DN.

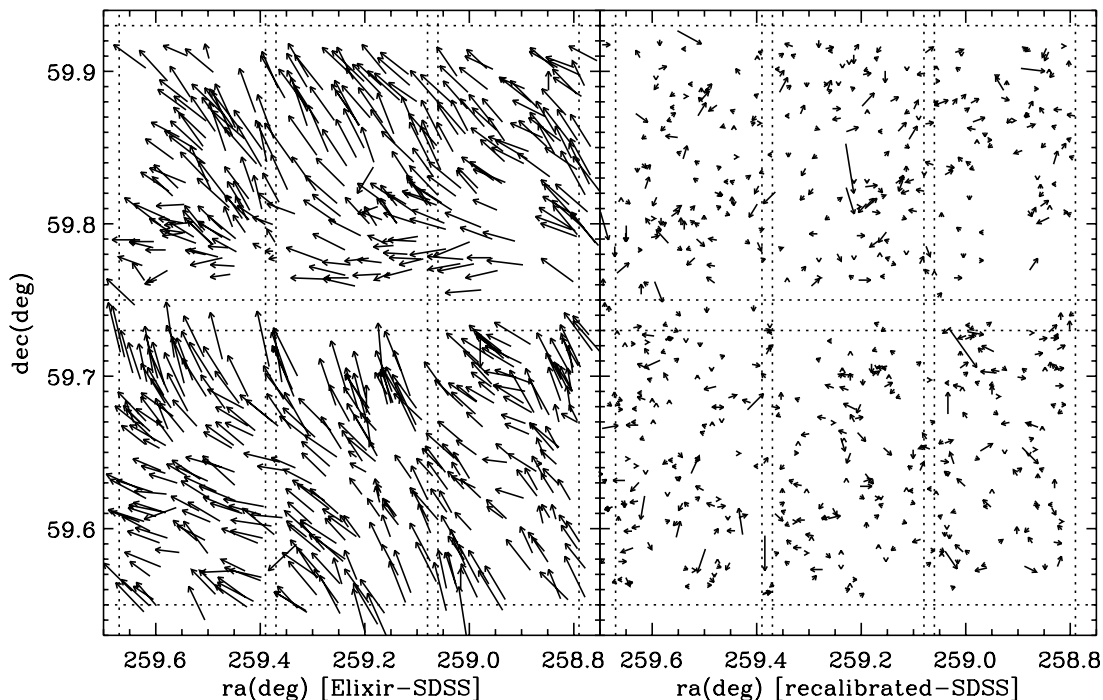


FIG. 3.—Improvement in astrometric solutions after the astrometric calibration with SDSS sources. The vectors indicate the difference between reference SDSS positions vs. detected positions. The size of the vectors are exaggerated by a factor of 250. The heads of the arrows point to SDSS positions. After the calibration, the size of the vectors remarkably decreased (by more than a factor of 5) and the distortion was reduced significantly. The figure represents six adjacent CCD chips. The borders of the CCD chips are shown as dotted lines.

image rotation are derived and written as World Coordinate System (WCS) keywords to the header of the raw image. Since the Elixir astrometric solution uses only a first-order fit, the absolute astrometric accuracy of the Elixir-processed images is about  $0''.5\text{--}1''$  rms with respect to the reference stars above. Final processed images are delivered to us as Multiple Extension Fits files that can be manipulated using IRAF<sup>7</sup> `mscred`.

### 3.2. Post-Elixir Processing before Mosaicking

The delivered images are processed before mosaicking, using various IRAF packages and tasks. The post-Elixir image processing includes (1) identification of saturated pixels and bleed trails; (2) creation of new bad pixel masks; (3) removal of satellite trails by inspecting each image frame; (4) replacement of bad pixel values; and (5) removal of cosmic rays.

As the first stage of the post-Elixir image processing, we identified saturated pixels and bleed trails using the `ccdproc` task in IRAF. The saturated pixels and bleed trails, which are the pixels showing nonlinear behavior, should be identified before stacking images because they can affect surrounding pixels during the projection of the image. Those pixels with values above the saturation level, 64,000 DN for the  $u^*$  band and 62,000 DN for the  $g$  band, were identified as saturated pixels. Neighboring pixels within a distance of 5 pixels along lines or columns of the selected saturation pixels are also identified as saturated. We found that the pixel saturation occurs typically at the central part of the stars brighter than  $u^* \simeq 20$  mag and  $g \simeq 21$  mag. Bleed trails, which result from charge spillage from a CCD pixel above its capacity, tend to run down the columns. We identify bleed trails as more than 20 connected pixels that are 5000 counts above the mean value along the whole image (i.e., setting the `ccdproc`

threshold parameter as “mean+5000”). After the identification of saturated pixels and bleed trails, this information is stored as a saturation mask.

Next, we used the IRAF task `imcombine` to make new bad pixel masks by combining the saturation masks with the original CFHT bad pixel masks. The resultant masks have pixel values of 0 for good pixels,  $>0$  for bad pixels. In the bad pixel masks, we also indicate the location of satellite trails. To include satellite trails in bad pixel masks, we identified satellite trails through the visual inspection by flagging their start and end  $(x, y)$  image coordinates and widths on each CCD chip. The flagged rectangular line is then marked as containing bad pixels in the bad pixel masks.

With the newly constructed bad pixel masks, we fixed the bad pixels using the IRAF `fixpix` task. The value of the pixel marked in the bad pixel masks was replaced by the linear interpolation value from adjacent pixels. The next step is to identify the pixels affected by cosmic rays. We applied a robust algorithm based on a variation of Laplacian edge detection with the program `la_cosmic` (van Dokkum 2001) on each CCD frame. This algorithm identifies cosmic rays of arbitrary sizes and shapes, and our visual inspection of this procedure confirms effective removal of cosmic rays. After the cosmic ray cleaning, we improved the astrometric solution, which is described in the next section.

### 3.3. Astrometric Calibration

The Elixir data pipeline performs a rough astrometric calibration on each image, and the existing header WCS keywords are updated with the improved astrometric solution. As mentioned in § 3.1, Elixir calculates the astrometric solution for each CCD chip. An initial guess is determined for the image coordinate based on the initial header WCS keywords, and Elixir uses the *HST* GSCs or USNO database to calculate an astrometric solution. The solution derived by Elixir is a first-order fit that gives the rms scatter of  $0''.5\text{--}1''$ . Thus, the solution is not good enough for

<sup>7</sup> IRAF is distributed by the National Optical Astronomy Observatory, which is operated by the Association of Universities for Research in Astronomy, Inc., under cooperative agreement with the National Science Foundation.

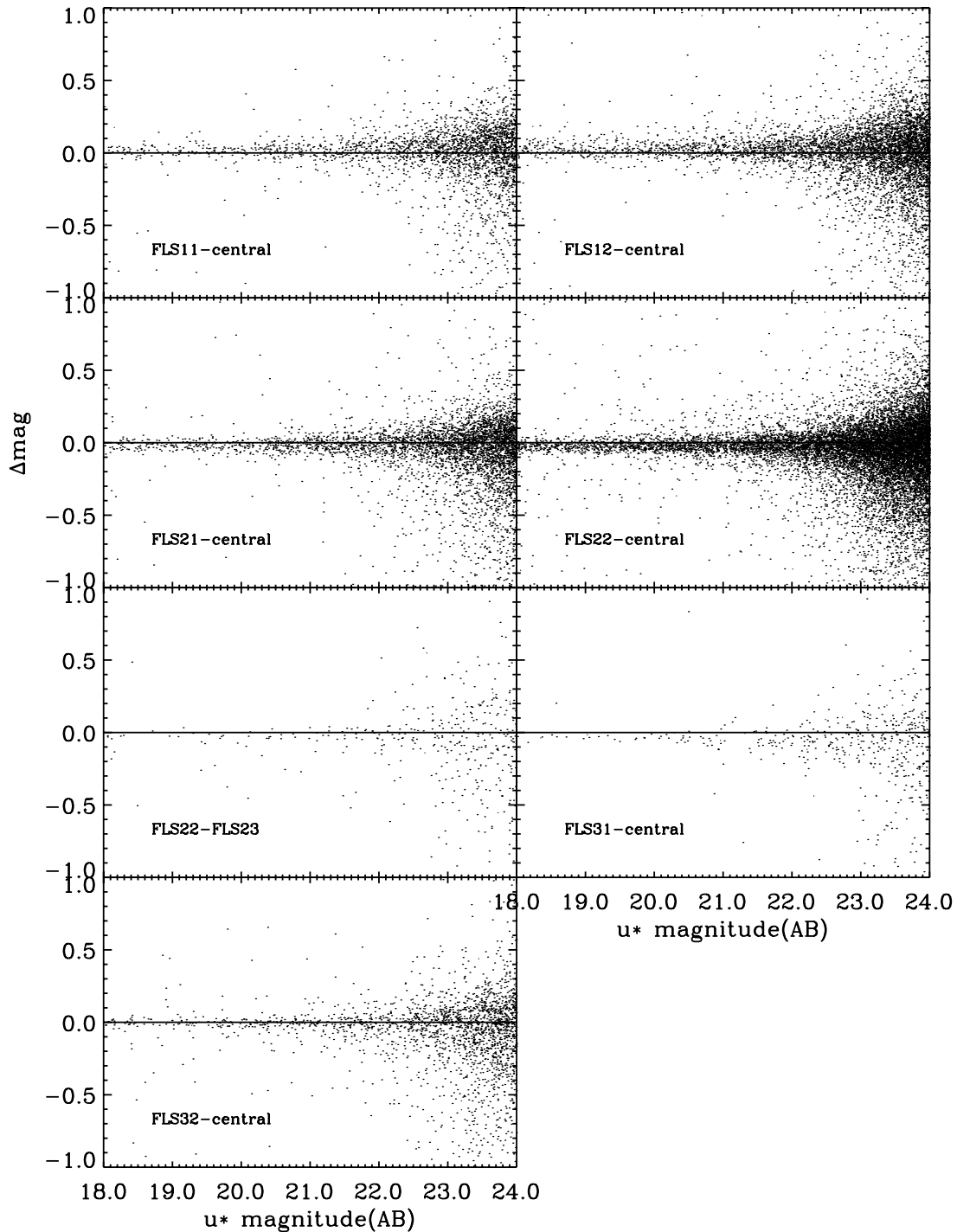


FIG. 4.—Magnitude difference of matched objects from different eight  $u^*$ -band fields before zero-point correction. Note that the objects lying in the FLS21, FLS22, and FLS31 fields are brighter than the objects lying in the central field before zero-point correction. The mean value of the magnitude offsets are FLS11 – central  $\simeq 0.006$ , FLS12 – central  $\simeq 0.018$ , FLS21 – central  $\simeq -0.028$ , FLS22 – central  $\simeq -0.029$ , FLS22 – FLS23  $\simeq -0.009$ , FLS31 – central  $\simeq -0.035$ , and FLS32 – central  $\simeq -0.001$ . Since the magnitude offsets of the FLS21, FLS22, and FLS31 fields are consistent within 0.01 mag, we used these fields as zero-point reference fields.

follow-up observations that require very accurate position information such as the multiobject spectroscopy. The accurate astrometry is also important when combining and mosaicking images, since misalignment of images can lead to a loss of signal in the combined image.

To improve the astrometric solutions, we adopted SDSS sources as reference points and derived the astrometric solution using the `msctpeak` task in `mscfinder`, which is a subpackage of the IRAF mosaic reduction package `mscred`. The SDSS sources brighter

than  $r \simeq 20$  mag have an absolute astrometric accuracy of  $0''.045$  rms with respect to USNO catalogs (Zacharias et al. 2000) and  $0''.075$  rms against Tycho-2 catalogs (Hog et al. 2000), with an additional  $0''.02$ – $0''.03$  systematic error in both cases (Pier et al. 2003). We also considered using USNO and GSC catalogs; unfortunately, many of the USNO and GSC stars were saturated in our images, making it difficult to use them for astrometric calibration.

There are other tasks such as `msczero` and `mscmatch` for deriving the astrometric solution, but we settled on using `msctpeak`.

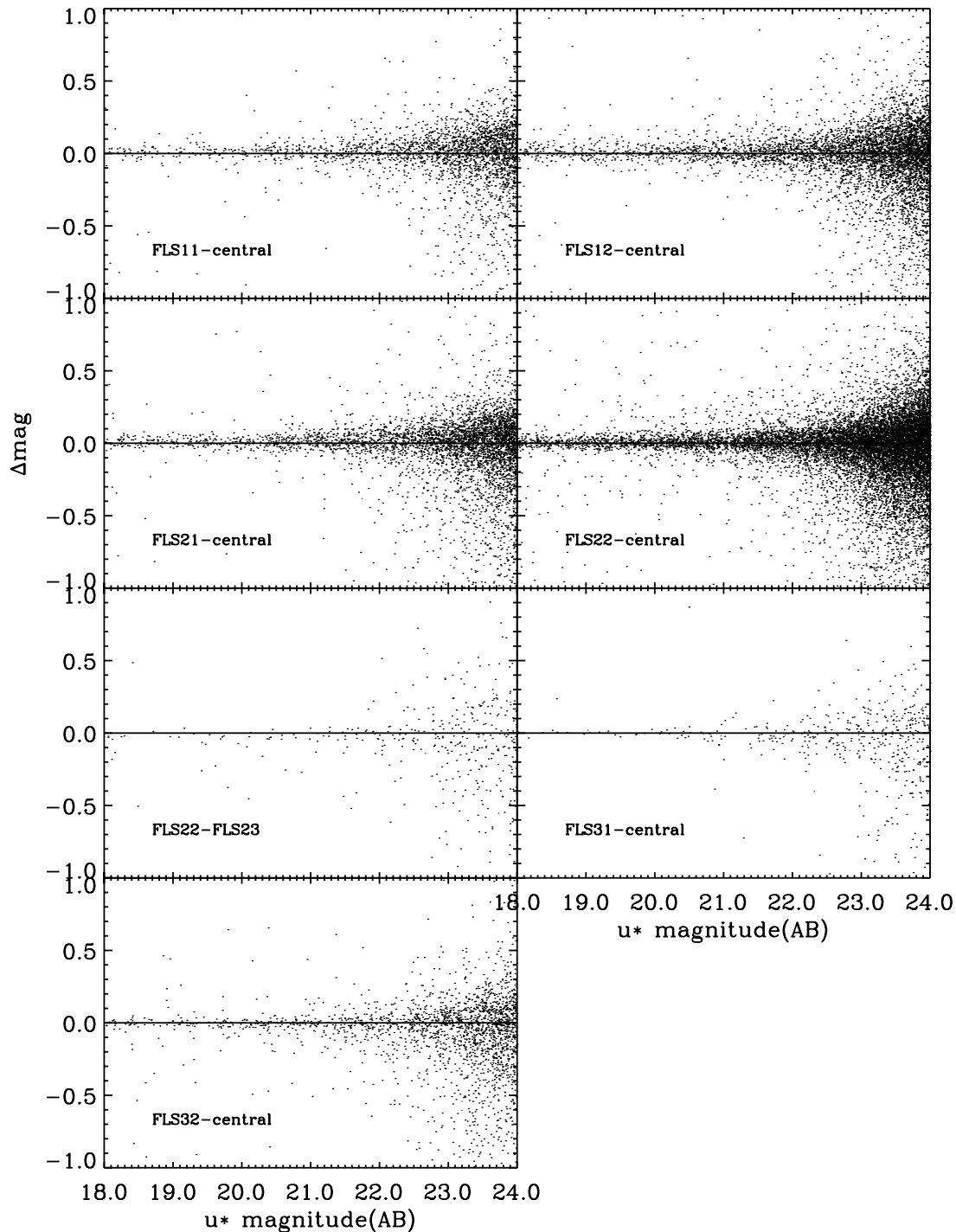


FIG. 5.—After the zero-point correction, the magnitude differences between fields are on the order of 0.01 mag.

Solutions from tasks such as `mscmatch`—which works only in TAN projection—are reflected in the value of `CDi_j`, `CRPIXi` header keywords. As a result, the astrometric solutions from such tasks have limitations and they do not improve the astrometric accuracy significantly. On the other hand, `msctpeak` creates a separate WCS database including a higher order fit solution from TNX sky projection geometry, and they are written as additional keywords such as `WATi_00j` in the FITS header using `mscsetwcs` task. The resultant astrometry of the image improved significantly over the original Elixir astrometry solution.

Ultimately, we used SDSS sources with  $16 \text{ mag} < u < 22 \text{ mag}$  and  $17 \text{ mag} < g < 22 \text{ mag}$  to calculate the astrometric solutions

for the  $u$ - and  $g$ -band images, respectively. The astrometric calibration objects were inspected by eye in order to exclude heavily saturated sources. The sources used for the astrometric calibration are not restricted to stars, since the SDSS filters and CFHT  $u^*$  and  $g$  filters are similar enough that the centroiding problem is not a great concern. Including both stars and galaxies, we could get  $\sim 90$  objects per chip to derive the astrometric solution. The solutions are calculated interactively for each chip; therefore, there are 36 solutions for each dither image. Functions used for the fitting are polynomials on the order 3–4, and the fitting errors are typically below  $0''.1$ . How the astrometric solutions are consistent with other data is described in a separate section (§ 5.1). Figure 3

demonstrates the improvement of astrometric solutions after executing the above procedure.

### 3.4. Production of Mosaic Images

We stacked the post-Elixir processed, astrometrically calibrated images using Swarp software by E. Bertin at TERAPIX (Traitement Elementaire, Reduction et Analyze des Pixels de megacam).<sup>8</sup> By running Swarp, we created the mosaic image and the corresponding weight image (coverage map) whose pixel value is proportional to the exposure time. The reduced images were resampled, background-subtracted, flux-scaled, and finally co-added to one image. The interpolation function we used in the resampling was LANCZOS3, which uses a moderately large kernel. The pixel scale of the resampled image was kept to the original MegaCam pixel size of  $0''.185$ . The astrometry transformation was handled by the Swarp program automatically, although the TNX WCS as derived in the previous section is not a FITS standard.

For the background subtraction, we used the background mesh size of  $128 \times 128$  pixels and applied a  $3 \times 3$  filter box. The background mesh size and the bin size were chosen to balance out the effect of bright stars (in general, smaller than  $128 \times 128$  pixels) and the effect of the overall background gradient. We tried many background combinations to obtain a background that was as flat as possible and settled on the above parameter values. The background-subtracted images were combined by taking the weighted average of each frame. The weight images were constructed by taking the bad pixel masks and replacing the bad pixel values with 0 and the good pixel values with 1. The weight images constructed in this way do not account for small variation in the pixel response over the CCD (flat field). Finally, the images were co-added using the following equation:

$$F = \frac{\sum w_i p_i f_i}{\sum w_i}.$$

In this equation,  $F$  is the value of a pixel in the final co-added image,  $w_i$  is the weight value for the pixel, and  $f_i$  is the value of the pixel in each individual image. The factor  $p_i$  represents the flux scale for each individual image. The images are calibrated to have the same photometric zero points after the Elixir pipeline, but due to the air mass differences, the flux scales of the images are slightly different. In order to take into account the difference in zero points, we set the flux scale of the image with the lowest extinction as 1.0. The flux scales of other images were calculated according to the equation

$$p_i = 10^{(k/2.5)(X_i - X_0)},$$

where  $k$  is the coefficient for the air mass term and  $X_0$  and  $X_i$  are air mass values of the reference image and the image in consideration, respectively. The co-added gain of the final stacked image varies with position and is proportional to the number of frames used for producing each co-added pixel value.

### 3.5. Photometric Calibration

We performed photometric calibration on the mosaic image of each field using the photometric solution provided by the Elixir pipeline. During the production of mosaic images (§ 3.4), we re-scaled each dithered image so that each co-added image has the photometric zero point of the image with the lowest air mass value. Then these magnitudes were corrected for Galactic extinction, estimating the amount of Galactic extinction from the ex-

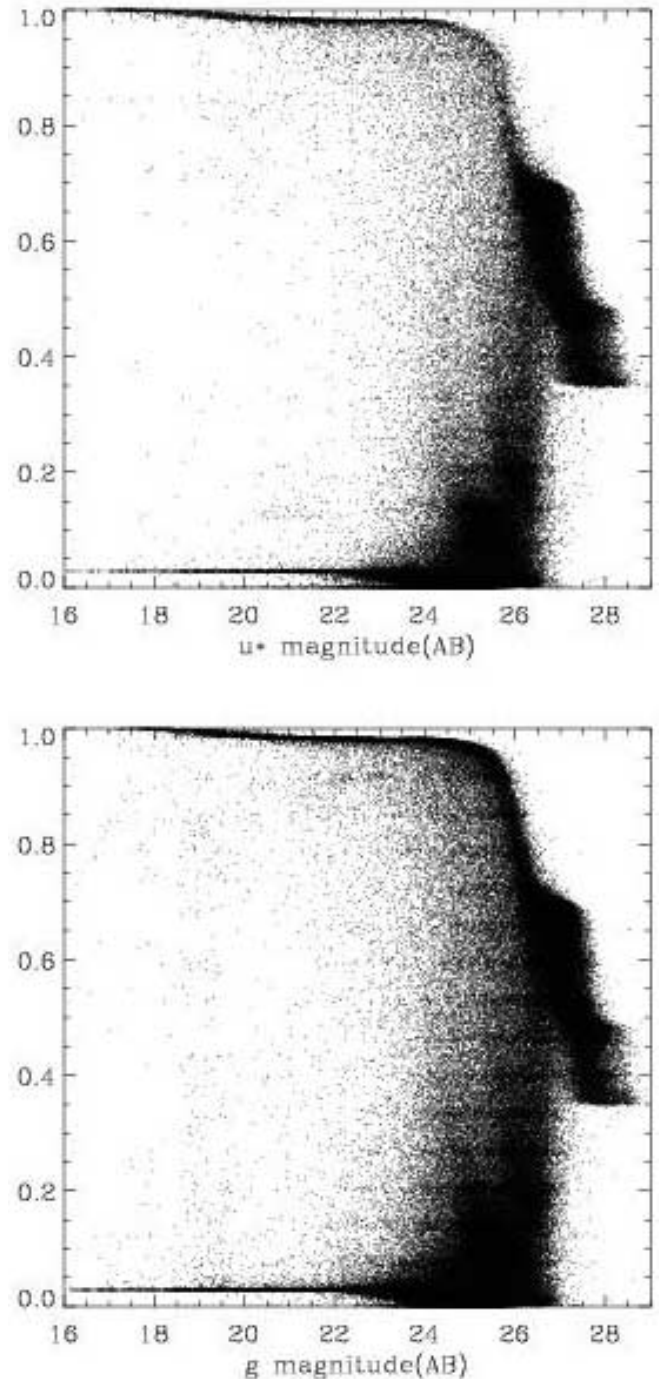


FIG. 6.—Distribution of the values of CLASS\_STAR parameter as a function of magnitude. At magnitudes below flux limit, the stellarity index of the objects is distributed between 0.35 and 0.7. The feature of the CLASS\_STAR distribution at faint objects ( $\leq 27$  mag) is due to the difficulties when calculating stellarity index with isophotal areas of the objects.

inction map of Schlegel et al. (1998). Since the FLS field lies at moderately high Galactic latitude, the amount of Galactic extinction is relatively small. They are 0.15 and 0.1 mag on average for the  $u^*$  and  $g$  bands, respectively. In the next step, we derived an additional zero-point correction necessary to account for some of the data that were taken under nonphotometric condition (e.g., thin cirrus).

To do so in the  $u^*$  band, we used fields whose mosaic image is made of photometric dither images only. The fields FLS21, FLS22, and FLS31 are such fields, and we used them as reference

<sup>8</sup> See <http://terapix.iap.fr>.

TABLE 3  
SELECTED 15 ENTRIES OF  $u^*/g$  BAND SOURCE CATALOG

ID	R.A. (J2000.0)	Decl. (J2000.0)	$u^*_{\text{AUTO}}^a$	$\epsilon$	$u^*_{\text{APER}}^b$	$\epsilon$	$g_{\text{AUTO}}$	$\epsilon$	$g_{\text{APER}}$	$\epsilon$	Star $_g^c$	Ext $_g^d$	Ext $_g$
1001.....	17 14 13.301	59 15 19.199	24.992	0.051	25.016	0.042	24.726	0.066	24.699	0.052	0.010	0.120	0.088
1002.....	17 17 11.895	59 15 27.342	24.882	0.043	25.200	0.052	24.834	0.063	25.112	0.073	0.006	0.169	0.125
1003.....	17 15 52.126	59 15 26.820	24.872	0.040	25.184	0.048	24.796	0.053	25.135	0.064	0.086	0.151	0.111
1004.....	17 13 19.966	59 15 16.411	24.955	0.050	25.408	0.061	24.582	0.069	25.144	0.092	0.024	0.114	0.084
1005.....	17 19 55.115	59 15 21.739	25.356	0.080	25.615	0.070	25.364	0.064	25.744	0.063	0.928	0.141	0.104
1006.....	17 14 53.745	59 15 25.502	25.628	0.088	26.223	0.156	25.666	0.071	26.027	0.102	0.586	0.124	0.092
1007.....	17 13 55.459	59 15 21.272	25.644	0.091	26.233	0.123	25.627	0.072	26.334	0.109	0.232	0.118	0.087
1008.....	17 18 35.120	59 15 27.905	26.073	0.138	27.508	0.390	26.164	0.110	28.560	0.752	0.725	0.158	0.116
1009.....	17 15 37.141	59 15 28.592	26.565	0.189	26.240	0.122	26.578	0.181	26.348	0.128	0.693	0.146	0.107
1010.....	17 15 33.977	59 15 19.844	23.060	0.009	24.161	0.019	22.738	0.013	23.741	0.026	0.028	0.145	0.106
1011.....	17 14 33.853	59 15 19.858	23.000	0.008	23.381	0.010	22.917	0.011	23.295	0.013	0.048	0.121	0.089
1012.....	17 17 52.075	59 15 25.035	23.869	0.018	24.589	0.030	23.858	0.037	24.674	0.068	0.029	0.180	0.132
1013.....	17 18 54.719	59 15 23.401	23.485	0.013	23.992	0.016	23.444	0.015	23.960	0.019	0.959	0.148	0.109
1014.....	17 16 11.917	59 15 26.175	23.960	0.018	24.495	0.025	23.890	0.023	24.382	0.031	0.036	0.153	0.113
1015.....	17 17 19.797	59 15 29.375	26.003	0.113	26.299	0.139	26.031	0.169	26.255	0.194	0.131	0.172	0.127

NOTE.—Units of right ascension are hours, minutes, and seconds, and units of declination are degrees, arcminutes, and arcseconds.

<sup>a</sup> The AUTO magnitudes are calculated by SExtractor, using Kron-like elliptical apertures (Kron 1980).

<sup>b</sup> The APER magnitudes are calculated over a circle with  $3''$  diameter.

<sup>c</sup> The stellarity represents CLASS\_STAR calculated with SExtractor. The values are distributed between 0 (galaxy) and 1 (star).

<sup>d</sup> The Galactic extinction values are calculated using the extinction map of Schlegel et al. (1998).

photometry fields to derive photometric zero-point correction of other  $u^*$ -band fields. Figure 4 shows the comparison of  $u^*$ -band magnitudes (before correcting for the nonphotometric data) between different fields that overlap with each other. For the comparison of magnitudes, we used the total magnitude (MAG\_AUTO) from SExtractor (see § 4). In Figure 4, we can see that  $u^*$ -band magnitudes of objects in FLS21, FLS22, and FLS31 fields are slightly brighter than the same objects in the central field. Also, objects in fields other than the reference photometry fields have  $u^*$ -band magnitudes similar to or fainter than those of the central field. The  $u^*$ -magnitude offsets between the central field and FLS21/FLS22/FLS31 are 0.03 mag and the rms in the offset values is on the order of  $\leq 0.01$  mag. This confirms that the  $u^*$ -band magnitudes of FLS21/FLS22/FLS31 fields are the most reliable. The final  $u^*$ -band zero points of each field are calculated using this strategy, and we present the zero points in Table 2. The comparison of  $u^*$ -band magnitudes of overlapping objects after the photometric calibration are presented in Figure 5. On the basis of the photometric consistency between FLS21/FLS22/FLS31, we estimate the accuracy of the  $u^*$ -band photometric zero point to be on the order of 0.01 mag.

For the  $g$ -band mosaic, we performed photometry on dither images that were taken under photometric conditions and derived a necessary zero-point correction by comparing the photometry of the mosaic image and the photometric reference image. The  $g$ -band zero point of the central field derived this way is also given in Table 2.

## 4. CATALOGS

### 4.1. Object Detection and Photometry

In the central  $1 \text{ deg}^2$  region (the 03B run), the stacked  $u^*$ - and  $g$ -band images were registered to the  $g$ -band image. Both bands have the same pixel scale, so they can be easily registered with the `xregister` task in IRAF. After the registration, source catalogs were created using dual-mode photometry with SExtractor (Bertin & Arnouts 1996). Specifically, objects were detected in the  $g$ -band image, and photometry was performed on both the  $g$ - and  $u^*$ -band images based on these positions. The weight

image (coverage map) produced by Swarp was used as the WEIGHT\_IMAGE. The LOCAL background is estimated using a  $128 \times 128$  pixel background mesh with  $3 \times 3$  median boxcar filtering, identical to the default Swarp settings.

We filtered our images with a Gaussian convolution kernel (`gauss_4.0_7x7.conv`) matched to our average seeing conditions (FWHM  $\sim 0''.85$ ). Finally, source detection was performed on the background-subtracted, filtered image by looking for pixel groups above the detection threshold. After playing with various parameter combinations and inspecting the results by eye, we settled on a minimum of eight connected pixels and a  $1.2 \sigma$  minimum detection threshold. We also tried various values for the deblending parameter to separate objects that are close together,

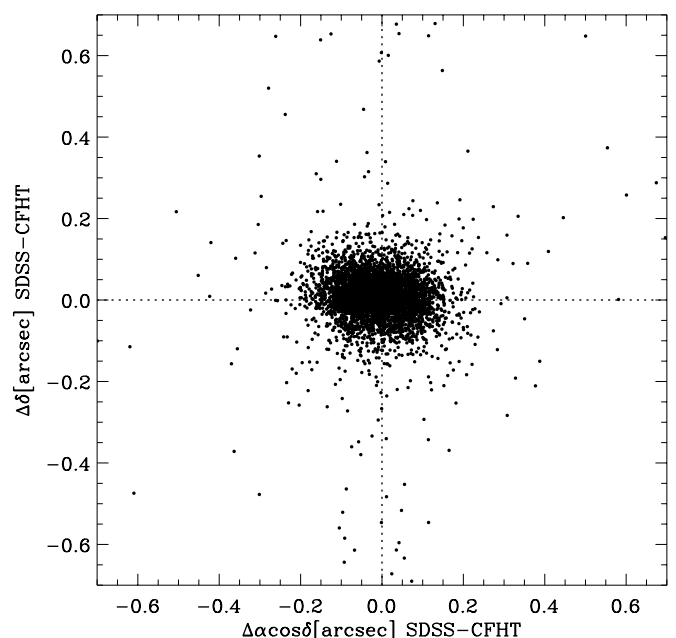


FIG. 7.— Comparison between the positions of matched objects in our  $g$ -band catalogs and SDSS  $g$ -band catalogs. Offsets are computed as SDSS minus CFHT positions.

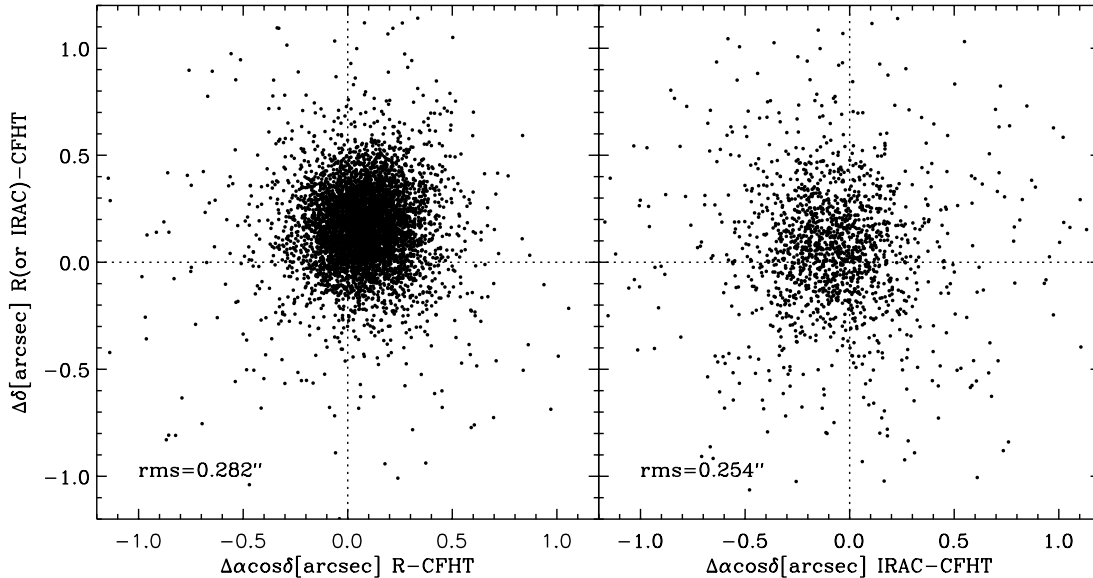


FIG. 8.— Comparison between the positions of matched objects in our  $u^*$ -band catalogs and  $R$ -band, IRAC catalogs. The offsets are computed as other survey minus CFHT positions.

and we adopted a deblending threshold of 32 and a deblending minimal contrast of 0.005.

Using dual-mode photometry, we detect  $\sim 200,000$  sources in the central  $1 \text{ deg}^2$  field. We also performed single-mode photometry on the  $u^*$ -band image with the same configuration file, to include  $u^*$ -band objects that are not detected in the  $g$  band. About  $\sim 150$  objects were detected in the  $u^*$  band without detection in the  $g$  band.

We applied a nearly identical method and parameters for source detection on the seven 04A FLS  $u^*$ -band images. Since there are several very bright stars in the 04A  $u^*$ -band images, we chose a bigger background mesh size,  $256 \times 256$  pixels, to avoid the oversubtraction of the background near bright stars. Since the seeing during 04A was slightly worse than that of 03B (Table 2), we adopted a slightly larger Gaussian convolution kernel (`gauss_5.0_9x9.conv`). As stated earlier, the gain for each stacked image is determined to be the original gain times the number of stacked images.

Due to interchip gaps and our  $30''$ – $40''$  dither steps, the effective exposure time varies from pixel to pixel. We therefore applied the Swarp weight image when performing photometry. Through the visual inspection of the weight image, we determined the value of `WEIGHT_THRESH` parameter for weighting in SExtractor. The value of the pixels in interchip gaps were measured and used as the threshold parameter value. This procedure prevents the rise of unusual sequence in the magnitude versus magnitude error plot.

In the catalogs, we present the apparent magnitude of the objects in two different ways (aperture and total magnitude). We measured the aperture magnitude using a  $3''$  diameter apertures. We adopted the auto magnitude (`MAG_AUTO`) from SExtractor as the total magnitude, which is calculated using the Kron elliptical aperture (Kron 1980). The related parameters, `PHOT_AUTOPARAMS` were determined to be 2.5 and 3.5, which are the values in the default configuration file.

#### 4.2. Star-Galaxy Separation

We use the SExtractor stellarity index to separate starlike objects from extended sources. SExtractor uses eight measured isophotal areas, peak intensity, and seeing information to calculate

the stellarity index. With the `SEEING_FWHM` parameter value and the neural network file as the inputs, SExtractor gives the stellarity index (`CLASS_STAR`), which has values between 1 (starlike object) and 0 as the result of the classification. Figure 6 shows the distribution of stellarity index as a function of magnitude in the central  $1 \text{ deg}^2$  field. We randomly picked objects with different apparent magnitudes and stellarity index values, and visually inspected them to see how useful the stellarity index is for the point source versus extended source classification. Our visual inspection reveals that bright objects ( $g < 21$  mag, and  $u^* < 20$  mag) with the stellarity index  $\geq 0.8$  are found to be stars. Through the visual inspection, we adopted the following criteria for separating point sources from extended objects: `CLASS_STAR`  $> 0.8$  for  $20 < u^* < 23$ ; `CLASS_STAR`  $> 0.8$  for  $21 < g < 23$ .

In addition to these criteria, we weed out bright saturated stars ( $g < 21$  mag,  $u^* < 20$  mag), based on SDSS point source catalogs. The subtraction of objects matched with SDSS stars is a good method for removing stars from our catalogs.

On the other hand, it is difficult to address the nature of faint ( $g > 23$  mag,  $u^* > 23$  mag) objects with the stellarity value alone, because faint, distant small galaxies are hardly resolved under  $1''$  seeing conditions. Fortunately, number counts tend to be dominated by galaxies at  $u^*$ ,  $g > 23$  mag. Therefore, we do not attempt to separate stars from galaxies at these flux levels. Also, the stellarity index distribution shows a converging feature between 0.35 and 0.7 at magnitudes below flux limit ( $g > 26.5$  mag,  $u^* > 26.2$  mag). This is thought to be the effect of difficulties in determining isophotal areas of faint objects.

#### 4.3. Catalog Formats

As an example, 15 entries of the central  $1 \text{ deg}^2$   $u^*$ - and  $g$ -band merged catalog is presented in Table 3. All magnitudes are given in the AB magnitude system. We include the total magnitude (`MAG_AUTO`) and the aperture magnitude ( $3''$  diameter) in the catalog. The magnitudes are not corrected for Galactic extinction, but the extinction values are presented as a separate column. Magnitude errors are the outputs from SExtractor. Considering the error in zero point and the extinction correction, we believe that the minimal error in the magnitude will be about

0.02 mag. Stellarity indices are calculated in the  $g$ -band image for the central field.

## 5. PROPERTIES OF THE DATA

### 5.1. Astrometry

We derived the final astrometric solution using SDSS sources (both point and extended sources). The rms error between SDSS point sources and our sources is calculated to be  $0''.1 < dr < 0''.15$ . Considering the absolute astrometric error of  $0''.1$  in SDSS (Pier et al. 2003), our catalogs are thought to have the positional error of roughly  $0''.15$ – $0''.2$ . Figure 7 shows the positional differences between SDSS sources and our sources over the entire mosaic of the central  $1 \text{ deg}^2$  field.

To address the accuracy of astrometric calibration in other ways, we compared our source positions with other available catalogs for the *Spitzer* FLS. The catalogs compared are KPNO  $R$ -band data (Fadda et al. 2004) and the *Spitzer* IRAC data (Lacy et al. 2005). The results are given in Figure 8. The average rms error,  $dr = (\Delta\alpha \cos \delta^2 + \Delta\delta^2)^{1/2}$ , is about  $\sim 0''.28$  with respect to  $R$ -band data.  $R$ -band positions have a systematic offset of  $\Delta\alpha = 0''.09 \pm 0''.27$  and  $\Delta\delta = 0''.19 \pm 0''.31$  with respect to CFHT positions. The systematic offset is originated from the fact that the reference catalog for  $R$ -band data is GSC II stars, which is known to have a systematic offset with respect to SDSS reference positions (Fadda et al. 2004). Therefore, we consider the astrometry difference between  $R$ -band and CFHT data to be well understood. For IRAC sources, the average rms error is  $dr \simeq 0''.25$ . The offset of IRAC positions according to CFHT positions are calculated to be  $\Delta\alpha = -0''.08 \pm 0''.40$  and  $\Delta\delta = 0''.04 \pm 0''.38$ . The FLS IRAC data have positional accuracy of  $0''.25$  rms with respect to 2MASS (Lacy et al. 2005). The difference between 2MASS positions and SDSS positions caused the offset between IRAC positions and CFHT positions. The results add support to the astrometric accuracy of our data set.

### 5.2. Photometry Transformation

As we have shown in Figure 1, MegaCam filters are slightly redder than their SDSS counterparts. Therefore, we examined the correlations between  $u^*$  magnitudes and SDSS  $u$  magnitudes. To do so, we matched nonsaturated point sources with  $18.5 < u < 20$  from our catalog with the SDSS point source catalog and compared the differences in their magnitudes. Figure 9 shows the comparison, and it demonstrates that the difference between the  $u^*$  and  $u$  bands varies from 0.1 to 0.6 mag as a function of the color of the object. We fitted the relation with a first-order polynomial to construct the conversion formula between CFHT  $u^*$  and SDSS  $u$ -band magnitudes and obtained the following relation from the linear least-squares fitting. Although there exists some scatter, the conversion formula could be a good reference in use of CFHT  $u^*$  magnitude:

$$\begin{aligned} \Delta\text{mag}(u_{\text{SDSS}} - u_{\text{CFHT}}) &= (-0.081 \pm 0.006) \\ &+ (0.237 \pm 0.004)(u - g)_{\text{SDSS}}. \end{aligned}$$

We checked the above empirical relation between MegaCam  $u^*$  and SDSS  $u$  by calculating  $u^* - u$  versus  $u - g$  using the filter curves in Figure 1 and the stellar templates from O5 V to F9 V stars (Silva & Cornell 1992), or the empirical galaxy templates at different redshift (Coleman et al. 1980). The theoretically calculated relations of  $u^* - u$  versus  $u - g$  agree well with the empirical relations (Figs. 10 and 11).

On the other hand, the difference between SDSS  $g$ -band magnitude and CFHT  $g$ -band magnitude is considerably small. Fig-

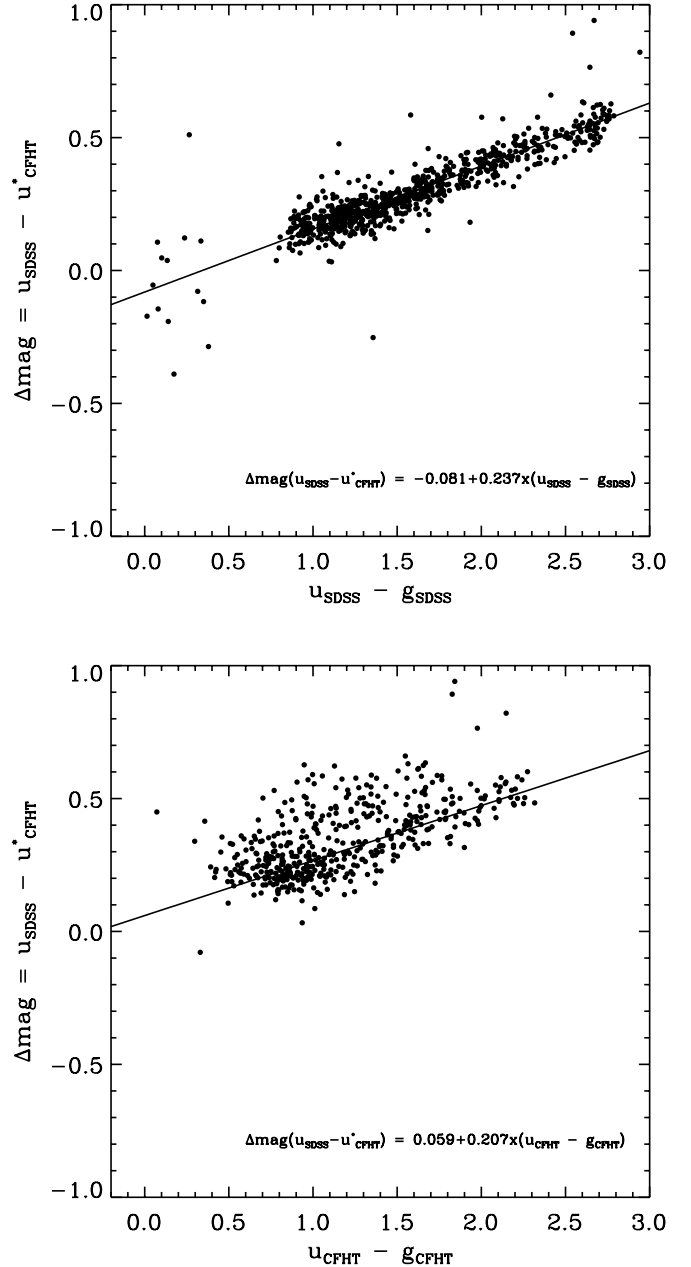


FIG. 9.—Empirical difference between CFHT  $u^*$ -band and SDSS  $u$ -band magnitudes as a function of  $u - g$  color. We used a least-squares fit to find the conversion equation from one  $u$  band to another.

ure 12 shows their difference along  $u - g$  color. Compared to Figure 9, the magnitude difference is small (they scatter within 0.15 mag), but the differences still have a tendency of increasing toward red color. We applied a least-squares fit to the  $g$ -band magnitude difference to find the following conversion relation:

$$\begin{aligned} \Delta\text{mag}(g_{\text{SDSS}} - g_{\text{CFHT}}) &= (-0.061 \pm 0.007) \\ &+ (0.057 \pm 0.004)(u - g)_{\text{SDSS}}. \end{aligned}$$

### 5.3. Galaxy Number Counts

To show the depth and homogeneity of the survey, we present the galaxy number counts in the  $u^*$  and  $g$  bands. The number counts are constructed for both the deep central  $1 \text{ deg}^2$  field and the shallower  $u^*$ -band coverage of the entire FLS fields. Then the results are compared with galaxy counts from other studies.

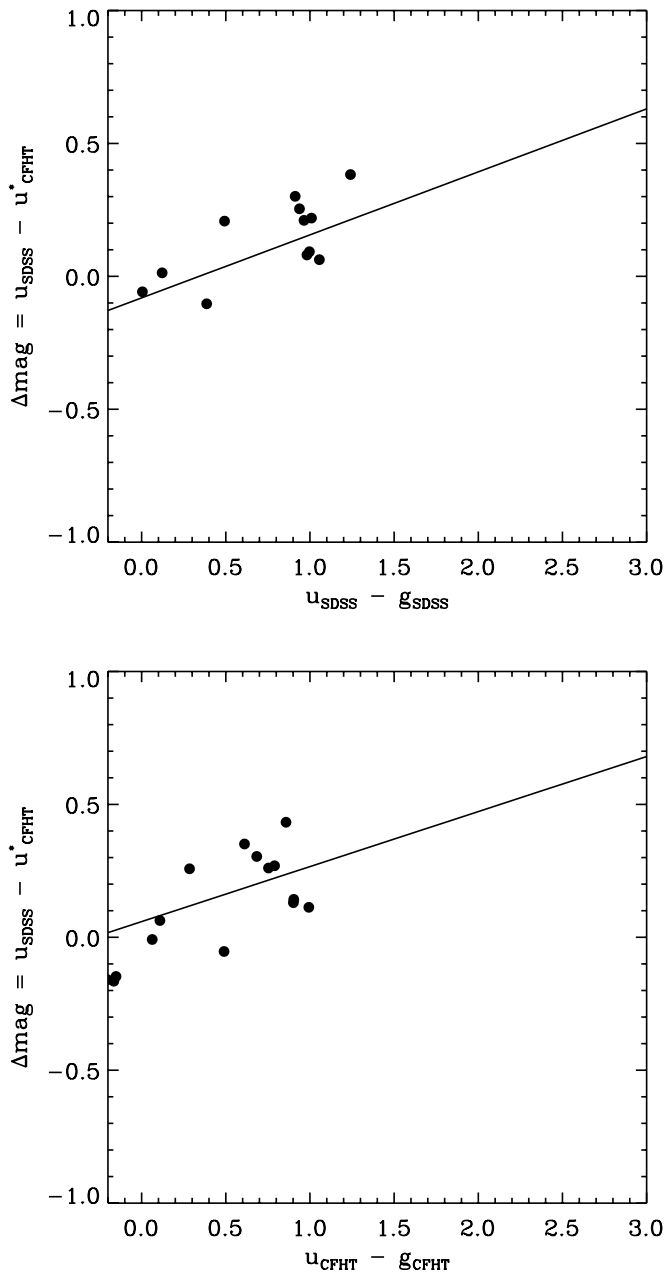


FIG. 10.—Calculated  $u^* - u$  for various spectral types of stars. The stellar templates from O5 V to F9 V stars were used in calculation, since in the case of red stars, the  $u$  band is not a good filter to sample their red colors.

The direct comparison is possible for the counts constructed from SDSS filters (Yasuda et al. 2001), while, for other studies using Johnson  $U$ , we converted the Johnson  $U$ -band magnitude to our  $u^*$  magnitude using the  $u - U \simeq 0.8$  conversion relation of galaxy colors from Fukugita et al. (1995) and then applying the mean of our empirical conversion relation between  $u^*$  and  $u$  ( $u^* - u = 0.4$  mag). For the  $g$  magnitude, we used  $B$ -band number counts from the literature (Metcalf et al. 2001; Capak et al. 2004; Arnouts et al. 2001; Huang et al. 2001), converting  $B$  magnitude to  $g$  magnitude according to the relation of  $g - B = 0.3 - 0.6$  (Fukugita et al. 1995). The conversion relation from Johnson  $U$  to  $u$  and from  $B$  to  $g$  filter varies according to the shape of the galaxy spectral energy distribution, so we adopt the mean difference to translate one filter to another.

The number counts are shown in Figure 13. When constructing the number counts, we excluded stellar objects using the

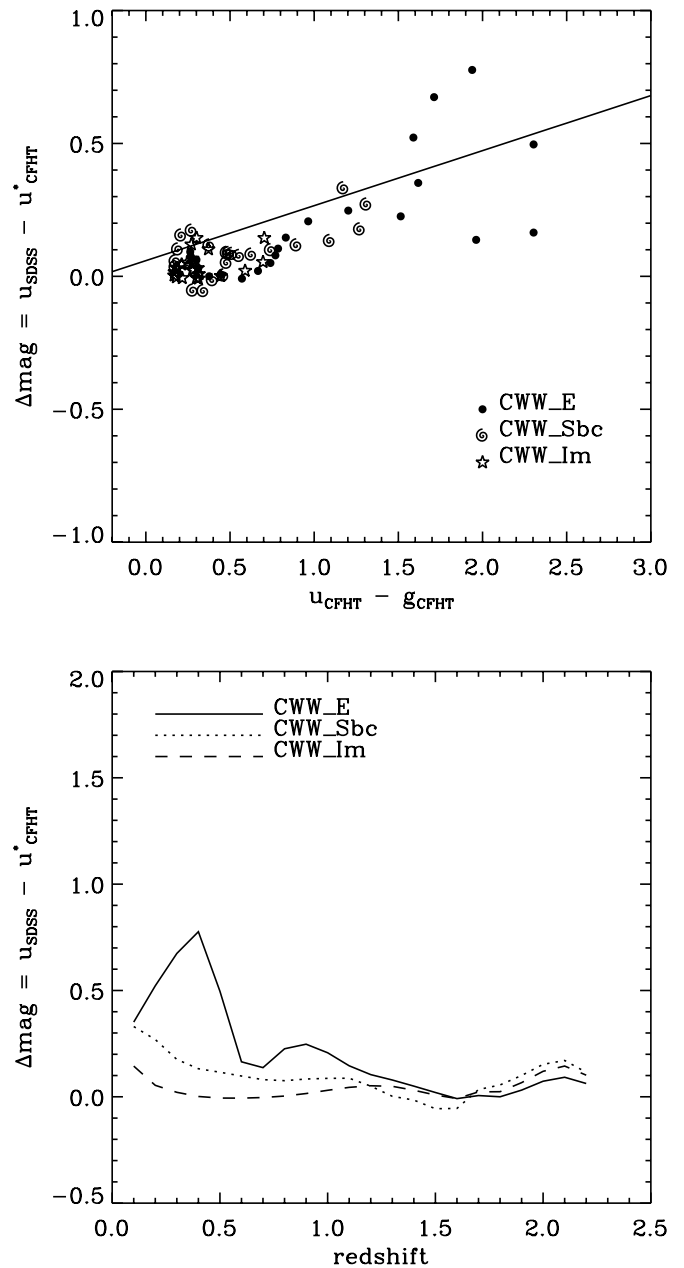


FIG. 11.—Calculated difference between the CFHT  $u^*$ -band and SDSS  $u$ -band magnitudes as a function of  $u - g$  color. The galaxy templates used are elliptical, spiral, and irregulars from Coleman et al. (1980). We redshifted the galaxies to various redshifts and calculated their colors using filter curves.

stellarity cut introduced in § 4.2. For objects brighter than  $g < 21$  mag and  $u^* < 20$  mag, we matched the SDSS point source catalogs with our catalogs and subtracted matched objects that are considered to be stars. Error bars on the figure represent the Poisson errors only. Also note that our counts are not corrected for completeness.

With the exception of SDSS studies (Yasuda et al. 2001), galaxy counts are typically derived from deep, but small area surveys ( $\sim 0.2 - 0.3$  deg $^2$ ). Our image covers from  $0.94$  deg $^2$  (in the case of the  $g$  band) to  $5.13$  deg $^2$  (in the case of the shallower  $u^*$  band). For  $u^* < 24$  mag, we include the shallower  $u^*$ -band data to maximize the area coverage. We can say that our number counts are better than other number counts in terms of the area coverage. For future use, we present a table that summarizes the result of galaxy number counts (Table 4). To construct the number

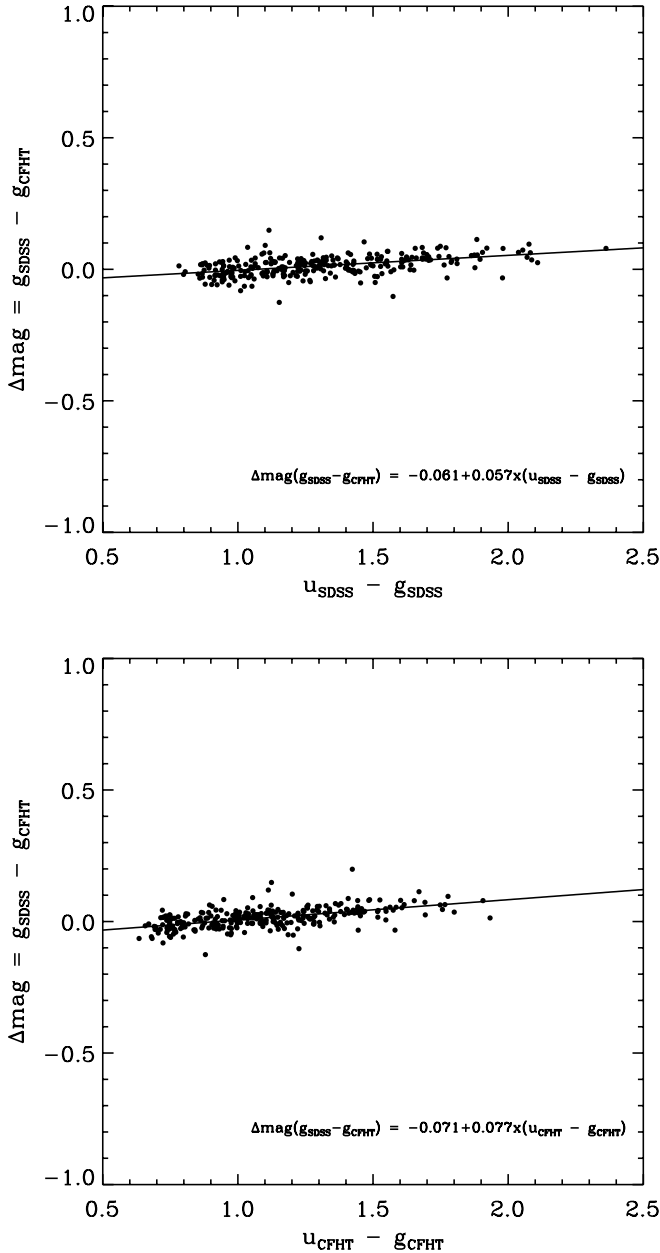


FIG. 12.—Empirical difference of CFHT  $g$ -band magnitude and SDSS  $g$ -band magnitude according to  $u - g$  color. Because the CFHT filter is redder than the SDSS filter, there is also a small tendency of magnitude difference along the color. But it is not difficult to say that the difference is negligible.

counts, we use the auto magnitude in SExtractor. Our number counts are in good agreement with the counts from other studies to  $u^* \simeq 24.8$  mag and  $g \simeq 25.2$  mag. Beyond  $u^* \simeq 24.8$  mag and  $g \simeq 25.2$  mag, our data start to tail off, and this shows that our  $u^*$  and  $g$  catalogs are nearly 100% complete down to the above magnitude limits. These limiting magnitudes have the uncertainty of 0.3 mag due to the fluctuation in the galaxy number counts at the faint end. We also obtained the number counts for the shallower  $u^*$ -band data, and the results are illustrated in Figure 14. In the case of the deepest field among the shallower  $u^*$  band, the 100% limit is 24.2 mag.

### 5.3.1. Completeness

To inspect the completeness of our survey in more detail, we used two independent methods. First, we compared our galaxy

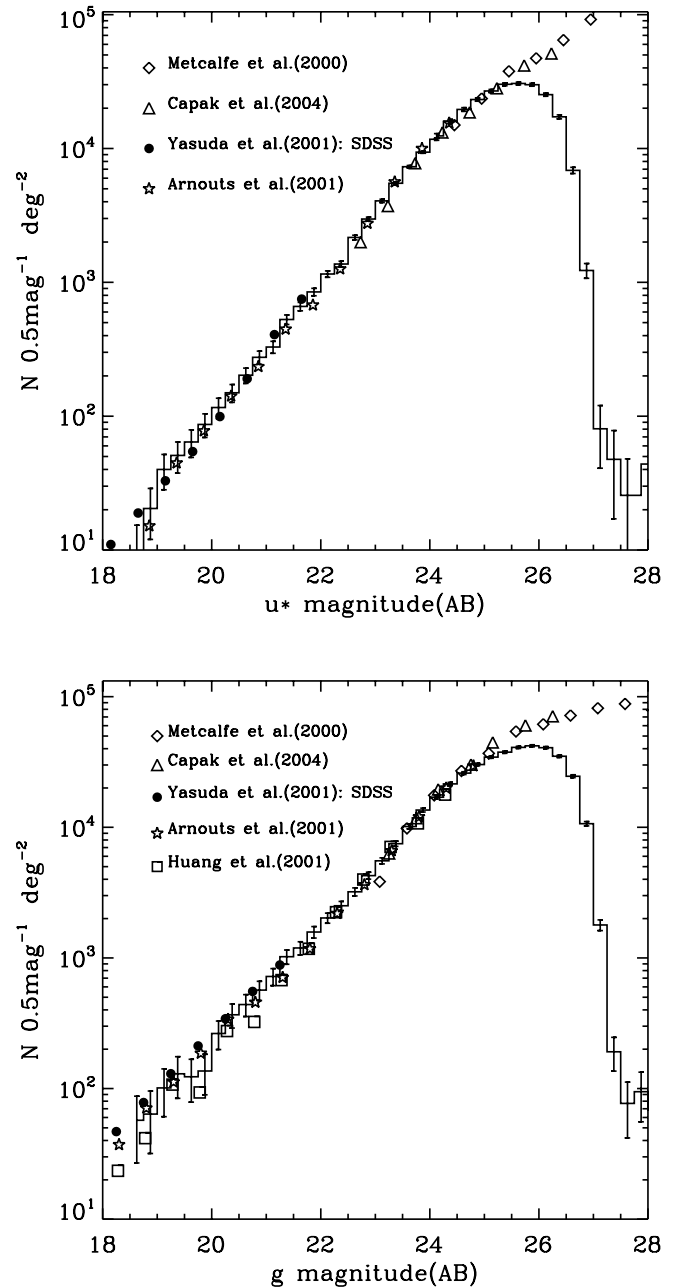


FIG. 13.—Galaxy number counts in FLS region from our  $u^*$ - and  $g$ -band images. Results from other studies are overplotted. Magnitudes are in AB system.

counts with the deeper galaxy counts from other studies. Second, we made artificial images having the same properties with our observation (seeing, crowding, gain, and background) using the `artdata` package in IRAF. The artificial image contained both point sources and extended sources. The extended sources are defined to have 40% of whole galaxies as elliptical galaxies and the remainders for disk galaxies, with minimum redshift of  $z \simeq 0.01$ . Poisson noise is added to the background. Then we performed photometry with the same configuration file we used to make catalogs of observed sources.

The results are shown in Figure 15, where the solid line and points indicate the completeness from the first method and the dashed line represents the completeness estimated from the simulation. Figure 15 shows that the data are 100% complete down to  $g \simeq 25.2$  mag and  $u^* \simeq 24.8$  mag, in agreement with the value

TABLE 4  
THE RESULT OF GALAXY NUMBER COUNTS

Magnitude (AB)	$\log N_{0.5}$ ( $0.5 \text{ mag}^{-1} \text{ deg}^{-2}$ )	Number of Galaxies	Area Coverage ( $\text{deg}^2$ )	$\log N_g$ ( $0.5 \text{ mag}^{-1} \text{ deg}^{-2}$ )	Number of Galaxies	Area Coverage ( $\text{deg}^2$ )
18.625.....	$0.933^{+0.061}_{-0.071}$	44	5.13	$1.743^{+0.060}_{-0.069}$	52	0.94
18.875.....	$1.272^{+0.042}_{-0.047}$	96	5.13	$1.790^{+0.057}_{-0.065}$	58	0.94
19.125.....	$1.555^{+0.031}_{-0.033}$	184	5.13	$1.991^{+0.046}_{-0.051}$	92	0.94
19.375.....	$1.659^{+0.028}_{-0.029}$	234	5.13	$2.099^{+0.041}_{-0.045}$	118	0.94
19.625.....	$1.760^{+0.025}_{-0.026}$	295	5.13	$2.076^{+0.042}_{-0.046}$	112	0.94
19.875.....	$1.891^{+0.021}_{-0.022}$	399	5.13	$2.120^{+0.040}_{-0.044}$	124	0.94
20.125.....	$2.017^{+0.018}_{-0.019}$	534	5.13	$2.407^{+0.029}_{-0.031}$	240	0.94
20.375.....	$2.127^{+0.016}_{-0.017}$	688	5.13	$2.551^{+0.025}_{-0.026}$	334	0.94
20.625.....	$2.258^{+0.014}_{-0.014}$	930	5.13	$2.629^{+0.023}_{-0.024}$	400	0.94
20.875.....	$2.392^{+0.012}_{-0.012}$	1266	5.13	$2.740^{+0.020}_{-0.021}$	516	0.94
21.125.....	$2.469^{+0.011}_{-0.011}$	1512	5.13	$2.844^{+0.018}_{-0.018}$	656	0.94
21.375.....	$2.675^{+0.009}_{-0.009}$	2426	5.13	$2.995^{+0.015}_{-0.015}$	930	0.94
21.625.....	$2.772^{+0.008}_{-0.008}$	3038	5.13	$3.062^{+0.014}_{-0.014}$	1084	0.94
21.875.....	$2.881^{+0.007}_{-0.007}$	3900	5.13	$3.184^{+0.012}_{-0.012}$	1436	0.94
22.125.....	$3.015^{+0.006}_{-0.006}$	5306	5.13	$3.292^{+0.011}_{-0.011}$	1840	0.94
22.375.....	$3.089^{+0.005}_{-0.006}$	6302	5.13	$3.385^{+0.010}_{-0.010}$	2282	0.94
22.625.....	$3.288^{+0.004}_{-0.004}$	9954	5.13	$3.492^{+0.008}_{-0.009}$	2920	0.94
22.875.....	$3.425^{+0.004}_{-0.004}$	13664	5.13	$3.616^{+0.007}_{-0.007}$	3884	0.94
23.125.....	$3.561^{+0.003}_{-0.003}$	18673	5.13	$3.729^{+0.006}_{-0.007}$	5042	0.94
23.375.....	$3.693^{+0.003}_{-0.003}$	25280	5.13	$3.860^{+0.006}_{-0.006}$	6816	0.94
23.625.....	$3.817^{+0.002}_{-0.002}$	33628	5.13	$3.992^{+0.005}_{-0.005}$	9224	0.94
23.875.....	$3.925^{+0.002}_{-0.002}$	43196	5.13	$4.118^{+0.004}_{-0.004}$	12334	0.94
24.125.....	$4.021^{+0.002}_{-0.002}$	53897	5.13	$4.216^{+0.004}_{-0.004}$	15464	0.94
24.375.....	$4.143^{+0.004}_{-0.004}$	13067	0.99	$4.320^{+0.003}_{-0.003}$	19652	0.94
24.625.....	$4.232^{+0.003}_{-0.003}$	16055	0.99	$4.411^{+0.003}_{-0.003}$	23648	0.94
24.875.....	$4.307^{+0.003}_{-0.003}$	19042	0.99	$4.506^{+0.003}_{-0.003}$	27510	0.94

found in the previous section, and are  $\sim 50\%$  complete to 26.5 mag for the  $g$  band and 26.2 mag for the  $u^*$  band.

For the shallower  $u^*$ -band data, we examined the completeness using the first method (see Fig. 16). The 50% complete limiting magnitudes are 24.8–25.4 mag, which are consistent with the estimated value in Table 2.

5.3.2. Reliability

We also examined the reliability of our detections. We created a negative image by multiplying  $-1$  to the mosaic image and performed photometry on the negative image. The number of objects detected in the negative image gives us an estimate of

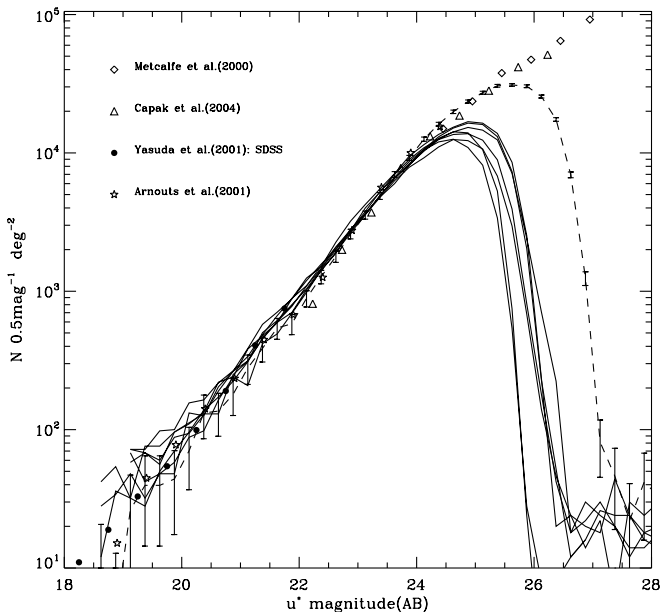


FIG. 14.—Galaxy number counts in FLS region from the shallower  $u^*$ -band images. Different solid lines indicate the different fields. The shallowest field (FLS23) shows 100% completeness to about 23.6 mag. The deepest field (FLS11) is 100% complete down to 24.2 mag. The dashed line shows the result from the central  $1 \text{ deg}^2$  region.

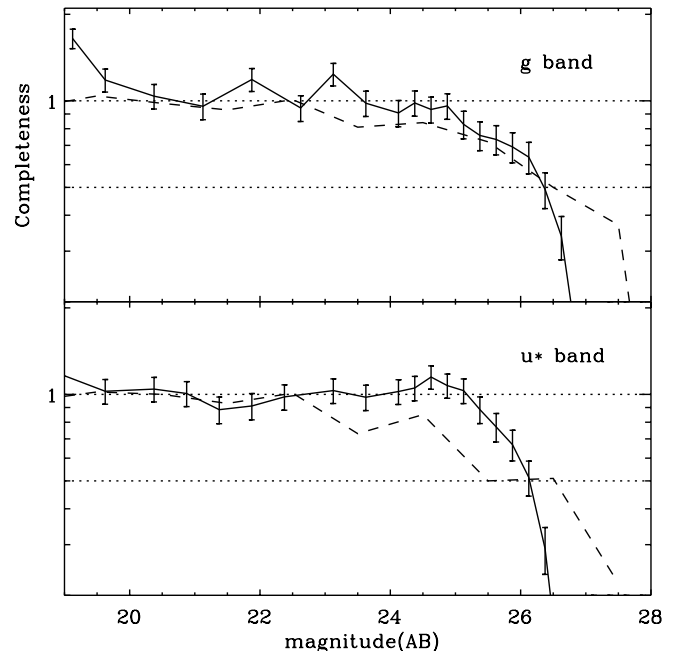


FIG. 15.—Completeness test. Completeness was inspected by dividing galaxy number counts with median number counts from other surveys (solid line). The dashed line shows the estimation of completeness from artificial image made.

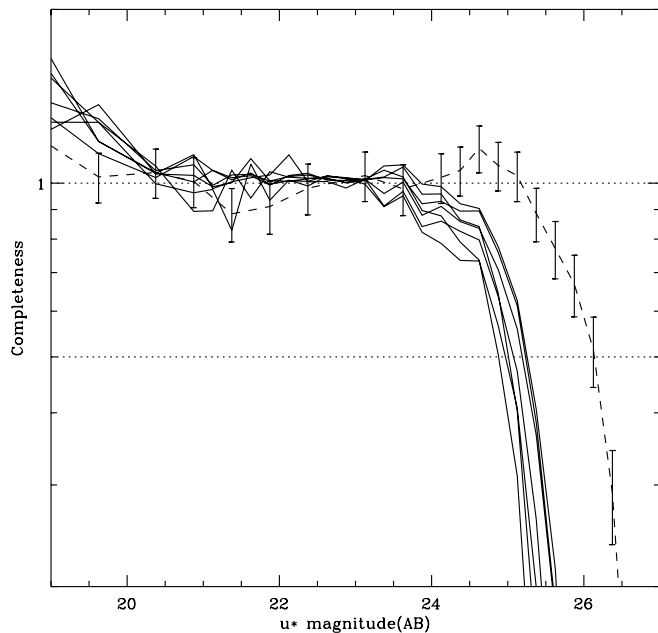


FIG. 16.—Completeness of the survey as a function of magnitude for the shallower  $u^*$  band. The dashed line shows the completeness of the central  $1 \text{ deg}^2$  region  $u^*$  band.

how many false detections exist in our catalogs. The false detection rate is defined as

$$\frac{N_{\text{false}}(m, m + \Delta m)}{N(m, m + \Delta m)},$$

where  $N_{\text{false}}(m, m + \Delta m)$  is the number of objects detected in the negative image over the magnitude bin of  $(m, m + \Delta m)$ , and  $N(m, m + \Delta m)$  is the number of objects detected in the original mosaic over the same magnitude bin. The false detection rate is 0.5, when there is only noise in the image.

The number of spurious detections are relatively small ( $< 0.7\%$ ) until  $g \simeq 26.5 \text{ mag}$  and  $u^* \simeq 26.0 \text{ mag}$ , when it increases steeply toward fainter magnitudes. The presence of false detections at brighter magnitudes (which is above the limiting magnitude) is due to the effects of streaks around bright stars. On the other hand, the majority of false detections at fainter magnitudes is generated from the noise. A similar tendency emerges on the shallower  $u^*$ -band images. The false detection rate remains under 1.8% until the limiting magnitudes for the shallower  $u^*$  band.

## 6. SUMMARY

The entire  $\sim 5 \text{ deg}^2$  region of the *Spitzer* First Look Survey area has been observed with the MegaCam on the CFHT 3.6 m telescope. From the data, we created nine final mosaic images, photometrically and astrometrically calibrated. Two of them are the deeper  $u^*$ - and  $g$ -band images of the central  $1 \text{ deg}^2$ , and the remaining seven are the shallower  $u^*$ -band images over the whole  $5 \text{ deg}^2$ . The average seeing for the central  $1 \text{ deg}^2$  field is  $0''.85$ , while the seeing is  $\sim 1''.00$  otherwise. The central field goes as deep as  $g \simeq 26.5 \text{ mag}$  and  $u^* \simeq 26.2 \text{ mag}$  at a  $5 \sigma$  flux limit within a  $3''$  aperture (or  $\sim 50\%$  completeness), while the shallower  $u^*$ -band data go to  $25.4 \text{ mag}$ . Our data are deep enough to detect optical counterparts of many IRAC and MIPS sources in the FLS region. We recalibrated the astrometric solution, and the final absolute astrometric uncertainty is at the level of  $0''.1$  when compared with SDSS point sources. With other surveys on FLS, the rms error is under  $0''.3$ , and it reflects merely the astrometric accuracy of the other data sets. The high astrometric accuracy allows this data to be used efficiently for multislit or fiber spectroscopic observation of faint galaxies in the FLS. Using dual-mode photometry, with the  $g$  band as the reference image, about 200,000 extragalactic objects were detected in our central  $1 \text{ deg}^2$  (effective observed area reaches  $\simeq 0.94 \text{ deg}^2$ ) down to  $g \simeq 26.5 \text{ mag}$ . There are  $\sim 50,000$  sources per  $\text{deg}^2$  in the shallower  $u^*$ -band images down to  $u^* \simeq 25.4 \text{ mag}$ . Our galaxy number counts are consistent with other studies, and the number of spurious detections is less than 0.7% below our limiting magnitudes. Our data could be used in many ways: for example, (1) selection of high-redshift objects using broadband dropout technique, (2) improvement of photometric redshifts, and (3) investigation on rest-frame UV properties of high-redshift infrared sources. These studies are currently under way. The mosaic images and catalogs will be available through a public Web site in the near future.

We acknowledge the FLS members for their support on this program, and Luc Simard and Tom Soifer for helping us to prepare the CFHT proposal. This work was supported by the University-Institute Cooperative Research Fund from the Korea Astronomy and Space Science Institute, and grant R01-2005-000-10610-0 from the Basic Research Program of the Korea Science and Engineering Foundation. We also acknowledge the hospitality of the Korean Institute of Advanced Study during the final stage of this work, and the support from the School of Earth and Environmental Sciences Brain Korea 21 program at Seoul National University.

*Facilities:* CFHT (MegaCam)

## REFERENCES

- Adelberger, K. L., & Steidel, C. C. 2000, *ApJ*, 544, 218  
 Appleton, P. N., et al. 2004, *ApJS*, 154, 147  
 Arnouts, S., et al. 2001, *A&A*, 379, 740  
 Bertin, E., & Arnouts, S. 1996, *A&AS*, 117, 393  
 Boulade, O., et al. 2003, *Proc. SPIE*, 4841, 72  
 Calzetti, D., Kinney, A. L., & Storchi-Bergmann, T. 1994, *ApJ*, 429, 582  
 Capak, P., et al. 2004, *AJ*, 127, 180  
 Choi, P. I., et al. 2006, *ApJ*, 637, 227  
 Coleman, G. D., Wu, C.-C., & Weedman, D. W. 1980, *ApJS*, 43, 393  
 Condon, J. J., Cotton, W. D., Yin, Q. F., Shupe, D. L., Storrie-Lombardi, L. J., Helou, G., Soifer, B. T., & Werner, M. W. 2003, *AJ*, 125, 2411  
 Fadda, D., Jannuzi, B., Ford, A., & Storrie-Lombardi, L. J. 2004, *AJ*, 128, 1  
 Fazio, G., et al. 2004, *ApJS*, 154, 10  
 Fang, F., et al. 2004, *ApJS*, 154, 35  
 Frayer, D. T., et al. 2004, *ApJS*, 154, 137  
 ———. 2006, *AJ*, 131, 250  
 Fukugita, M., Shimasaku, K., & Ichikawa, T. 1995, *PASP*, 107, 945  
 Hog, E., et al. 2000, *A&A*, 357, 367  
 Huang, J.-S., et al. 2001, *A&A*, 368, 787  
 Kennicutt, R. C., Jr. 1998, *ARA&A*, 36, 189  
 Kron, R. G. 1980, *ApJS*, 43, 305  
 Lacy, M., et al. 2004, *ApJS*, 154, 166  
 ———. 2005, *ApJS*, 161, 41  
 Marleau, F. R., et al. 2004, *ApJS*, 154, 66  
 Metcalfe, N., Shanks, T., Campos, A., McCracken, H. J., & Fong, R. 2001, *MNRAS*, 323, 795  
 Meurer, G. R., Heckman, T. M., & Calzetti, D. 1999, *ApJ*, 521, 64  
 Morrison, J. E., et al. 2001, *AJ*, 121, 1752

- Oke, J. B. 1974, ApJS, 27, 21  
Pier, J. R., et al. 2003, AJ, 125, 1559  
Rieke, G. H., et al. 2004, ApJS, 154, 25  
Schlegel, D. J., Finkbeiner, D. P., & Davis, M. 1998, ApJ, 500, 525  
Silva, D. R., & Cornell, M. E. 1992, ApJS, 81, 865  
van Dokkum, P. G. 2001, PASP, 113, 1420  
Yan, L., et al. 2004a, ApJS, 154, 60  
———. 2004b, ApJS, 154, 75  
Yasuda, N., et al. 2001, AJ, 122, 1104  
Zacharias, N., et al. 2000, AJ, 120, 2131